LA-UR-01-3019
Approved for public release;
distribution is unlimited.

Title: **MULTI-COMPONENT GAS TRANSPORT IN CANDU FUEL RODS DURING SEVERE ACCIDENTS**

Author(s): B. Szpunar, B.J. Lewis, V.I. Arimescu, R.S.Dickson, L.W. Dickson and M.I. Baskes

Submitted to:

http://lib-www.lanl.gov/la-pubs/00818639.pdf

MULTI-COMPONENT GAS TRANSPORT IN CANDU FUEL RODS DURING SEVERE ACCIDENTS

B. Szpunar[1], B.J. Lewis[1], V.I. Arimescu1[1*], R.S.Dickson[2], L.W. Dickson[2] and M.I. Baskes[3]

[1]Royal Military College of Canada, Department of Chemistry and Chemical Engineering
P.O. Box 17000 St. Forces, Kingston, Ontario, CANADA K7K 7B4
[2]Atomic Energy of Canada Limited , Chalk River Laboratories
Chalk River, Ontario, CANADA K0J 1J0
[3]Los Alamos National Laboratory, MST-8, MS G755, Los Alamos, NM 87545

ABSTRACT

The multi-component transport of steam, hydrogen and stable fission gas in the fuel-to-clad gap of defective CANDU fuel rods, during severe accident conditions, is investigated. Based on a general Stefan-Maxwell treatment this work considers how incoming steam will diffuse into a breached rod against a counter-current flow of non-condensable fission gases and out-flowing hydrogen that is produced from the internal reaction of steam with the Zircaloy cladding or urania. The ability of the oxidized clad to act as a physical barrier to either hydrogen or oxygen diffusion was further investigated in the current work with a molecular-dynamics approach, with the interactions between atoms represented by a Modified Embedded Atom Method.

During the initial Zircaloy oxidation phase in the CRL experiments, the model was able to predict the reduced fission product release kinetics as well as the timing for the completion of the clad-oxidation process. In this simulation, the model (with an effective gap size of 20 μm) was able to successfully predict whether single-sided or double-sided oxidation had occurred in accordance with the metallographic examination. However, in order to account for the observed release kinetics after the completion of clad oxidation, it was necessary to assume a greater atmospheric exchange due to possible cracking of the brittle oxide layer. With the assumption of cracking (by assuming a reduced path length for gas transport), the model was successfully able to reproduce the fission product release kinetics and the final fuel stoichiometry as determined from end-of-test weight gain measurements.

This analysis particularly shows that local hydrogen production (from the internal fuel oxidation process) will result in a reduced local oxygen potential in the fuel-to-clad gap compared to that which occurs in the bulk coolant.

1. INTRODUCTION

The transport of the short-lived volatile fission products in the gap has been studied extensively during normal reactor operation, where diffusion is shown to be the dominant process of transport in the fuel-to-clad gap.[1-5] During a high-temperature reactor transient, if the heat-up rate of the fuel rod is typically less than <0.5 K/s, the fuel cladding is completely oxidized to ZrO_2 under steam-rich conditions before reaching the melting point of metallic Zircaloy.[6] Although the cladding is embrittled due to the oxidation process, it will remain in place and act as a physical barrier unless the ZrO_2 shell is compromised as result of rod fragmentation by mechanical stress or chemically dissolved by molten material.[6] In the event that the ZrO_2 shell remains in place, an enhanced stable gas release from the fuel matrix into the fuel-to-clad gap at the higher temperature may lead to a pressure differential between the internal rod atmosphere and the bulk coolant (i.e., the bulk coolant system pressure will decrease with coolant blowdown). As such, bulk convection of fission gases in the gap could also occur as a transport process.[5,7] During the oxidation of the internal and external Zircaloy cladding surfaces, hydrogen will be generated which will initially lower the oxygen potential in the bulk coolant and locally in the fuel-clad gap. Thus, any incoming steam into a breached rod must diffuse against a counter-current flow of non-condensable fission gases (as released from the fuel matrix), and any out-flowing hydrogen that is produced from internal reaction of the in-coming steam with the Zircaloy cladding or urania.[8]

---

[*] Present Address: Siemens Power Corporation, P.O. Box 130, Richland, WA 99352-0130

It is important to determine the molar concentration distribution along the gap for this multi-component mixture (i.e., consisting of steam, hydrogen and fission gas) since the oxygen potential in the gap will depend on the local constituent partial pressures. The oxygen potential is an important parameter since it will dictate the fuel oxidation state, and hence the rate of fission-product diffusion in the fuel matrix and the subsequent volatile fission product release into the gap.[9] In addition, the oxygen partial pressure is a boundary condition that controls the amount of fuel volatilization (i.e., formation of gaseous UO_3 and $UO_2(OH)_2$), as well as the chemical form of the fission products themselves in the fuel matrix.[10-13] This chemical speciation will specifically determine the amount of vaporization of the low-volatile fission products from the fuel surface.[10,13] Thus, for a proper simulation of the fuel and fission product release behavior during a severe accident, the oxygen potential must be known *a priori*.

As previously mentioned, earlier analyses have principally focused on fission-product transport in the gap (in accordance with binary diffusion of a trace fission product species diffusing in a continuum steam medium, and the possibility of bulk-convective transport with pressure differential).[5,7] Although multi-component transport in the gap of breached rods has been considered for severe accident conditions, this work did not specifically consider oxygen potential effects (i.e., it was implicitly assumed that the breached site becomes a source of hydrogen due to steam reaction with the cladding).[14] In other work, the effect of a reduced oxygen potential in the gap was modelled by simply reducing the oxygen potential in the bulk coolant by an empirical factor; i.e., this factor was derived by matching the predicted fuel oxidation kinetics to the observed end-state weight gain for the test rods in specific high-temperature annealing experiments.[9] In contrast, in the current work, the general mathematical model of Ref. 8 is adopted for the complete description of the multi-component transport of steam, hydrogen and fission gas in the fuel-to-clad gap of a breached fuel rod in which the resultant ZrO_2 layer, produced by metal-water reaction at high temperature, can inhibit steam penetration into the fuel rod. The numerical solution of the generalized transport equations is detailed in the current work based on a finite difference and control volume approach with a sparse matrix scheme to reduce the computational requirements.

The solution of the transport equations provides the time-dependent molar distributions of steam, hydrogen and fission gas components in the fuel-to-clad gap from which the oxygen potential can be directly estimated. The present model is specifically applied to the simulation of three annealing experiments conducted in steam at the Chalk River Laboratories (CRL) from 1628 to 1915 K, using short-length spent fuel samples with Zircaloy cladding. The current model is used to interpret the observed fission product (i.e., cesium) release, and the Zircaloy and urania oxidation behavior.

2. MODEL DEVELOPMENT

2.1 Gap Transport Equations

A one-dimensional model can be considered for the transport of steam, hydrogen and stable fission gas in breached fuel rods during accident conditions since, in the absence of significant clad ballooning, the annular gap between the fuel and cladding is quite thin compared to the axial transport path length. In the development of this model, it is assumed that a breach is present at the down-stream end of the rod as shown in Fig. 1. The gap transport equations for this multi-component mixture follows from the conservation equation:[15]

$$\frac{\partial c_i}{\partial t} = -\frac{\partial N_i}{\partial z} + q_i - r_i . \tag{1}$$

Here for a given component i, c_i (mol m^{-3}) is the molar concentration, N_i is the molar flux in the z-direction (mol m^{-2} s^{-1}) (resulting from diffusion and a total bulk molar flow), and q_i and r_i are the production and loss rates, respectively (in mol m^{-3} s^{-1}). For the evaluation of the molar flux with an ideal gas mixture of n components, the Stefan-Maxwell equations are employed:[15]

$$\frac{\partial y_i}{\partial z} = \sum_{j=1, j\neq i}^{n} \frac{1}{cD_{ij}} \left[y_i N_j - y_j N_i \right] \tag{2}$$

Here c is the total molar concentration

$$c = \sum_{j=1}^{n} c_j , \tag{3}$$

and y_i (= c_i/c) is the mole fraction of species i. The diffusivity D_{ij} (m^{-2} s^{-1}) of the i-jth pair is evaluated for the binary mixture with Chapman-Enskog kinetic theory[8].

For the current problem, in addition to the components of the bulk atmosphere (steam and hydrogen), there is also a release of fission gas from the fuel into the gap, which can be represented by xenon. Thus, as detailed in Ref. 8, the Stefan-Maxwell equations in Eq. (2) can be used to relate the molar fluxes to the concentration gradient of the mole fractions, which results in an expression for N_i in Eq. (1). Consequently, a set of coupled equations for the multi-component mixture follows (i.e., where 1 = Xe, 2 = H_2O and 3 = H_2):[8]

$$c\frac{\partial y_1}{\partial t} = \frac{\partial}{\partial z}\left[c\left(Đ_{11}\frac{\partial y_1}{\partial z} + Đ_{12}\frac{\partial y_2}{\partial z} \right)\right] - N_T \frac{\partial y_1}{\partial z} + (1-y_1)q_1(z,t) \tag{4a}$$

$$c\frac{\partial y_2}{\partial t} = \frac{\partial}{\partial z}\left[c\left(Đ_{21}\frac{\partial y_1}{\partial z} + Đ_{22}\frac{\partial y_2}{\partial z} \right)\right] - N_T \frac{\partial y_2}{\partial z} - y_2 q_1(z,t) - r_2^{\text{clad ox}}(z,t) - r_2^{\text{fuel ox}}(z,t) \tag{4b}$$

$$y_3 = 1 - y_1 - y_2 . \tag{4c}$$

For this ternary system (i.e., H_2O-H_2-Xe mixture), only two equations are independent (i.e., Eqs. (4a) and (4b)), due to the constraint that the mole fractions must sum to unity as shown in Eq. (4c). The source term due to stable fission gas release into the gap (q_1) and the loss terms due to steam oxidation with the fuel ($r_2^{\text{fuel ox}}$) and the Zircaloy cladding ($r_2^{\text{clad ox}}$) are detailed in Section 2.2. The multicomponent diffusion coefficients are defined as:

$$Đ_{11} = \frac{Y_{12} + Y_{32} + Y_{23}}{\det}, \quad Đ_{12} = \frac{Y_{12} - Y_{13}}{\det}, \quad Đ_{21} = \frac{Y_{21} - Y_{23}}{\det}, \quad Đ_{22} = \frac{Y_{21} + Y_{31} + Y_{13}}{\det} \tag{5a}$$

where

$$\det = \frac{y_1}{D_{12}D_{13}} + \frac{y_2}{D_{12}D_{23}} + \frac{y_3}{D_{13}D_{23}} \text{ and}$$

$$Y_{12} = \frac{y_1}{D_{12}}, \quad Y_{13} = \frac{y_1}{D_{13}}, \quad Y_{21} = \frac{y_2}{D_{12}}, \quad Y_{23} = \frac{y_2}{D_{23}}, \quad Y_{31} = \frac{y_3}{D_{13}}, \quad Y_{32} = \frac{y_3}{D_{23}}. \tag{5b}$$

The total molar flux $N_T = N_1 + N_2 + N_3$, is derived from a total gas balance:

$$\frac{\partial c}{\partial t} = -\frac{\partial N_T}{\partial z} + q_1 . \tag{6}$$

In Eq. (6), the source of gas q_1 is attributed to xenon since there is no net gain of gas for steam and hydrogen due to the equal molar production and loss of these species in the oxidation reactions of the clad and fuel (see Section 2.2.2).

The initial and boundary conditions for the transport equations are

$$y_1 = y_1^o, \quad y_2 = y_2^o, \quad \text{for} \quad t = 0, \quad 0 < z < L \tag{7a}$$

$$\frac{\partial y_1}{\partial z} = \frac{\partial y_2}{\partial z} = 0, \quad \text{for} \quad z = 0, \quad t > 0 \tag{7b}$$

$$y_1 = 0, \quad y_2 = y_2^c(t), \quad \text{for} \quad z = L, \quad t > 0 \tag{7c}$$

The quantities y_1^o and y_2^o in Eq. (7a) are the initial quantities of xenon and steam present in the gap at the start of the transient for a given accident scenario. The reflexive conditions in Eq. (7b) indicate no flow at the intact end of the fuel rod in Fig. 1. The boundary condition at the breached end in Eq. (7c) indicates a zero concentration of fission gas since it is continually being swept away by the bulk gas atmosphere flowing past the fuel rod. On the other hand, there is a constant supply of steam (with a mole fraction $y_2^c(t)$) at this exposed end from the reactor coolant system (RCS) (see Section 2.4).

During a reactor transient, a temperature gradient may be present in the fuel rods so that the temperature profile $T(z,t)$ must be known for solution of the gap transport equations (based on previous reactor safety calculations). In addition, a pressure gradient may also arise along the gap due to the continual release of stable fission gas into the gap.[5,7] Considering these effects, the molar concentration can be generally derived from the ideal gas law:

$$c(z,t) = \frac{P(z,t)}{RT(z,t)} \tag{8}$$

where R is the ideal gas constant. For determination of the pressure gradient, the momentum equation can be approximated by a steady-state Hagen-Poisseulle solution for laminar flow, where the bulk mass average velocity (u) is related to the pressure gradient (dP/dz) via:[5]

$$u + \frac{h^2}{12\mu}\frac{dP}{dz} = 0 \tag{9}$$

where μ is the viscosity of the gas mixture and h is the radial gap thickness. Furthermore, assuming that the bulk molar velocity (v) is equal to the bulk mass average velocity (u) then $N_T = cu$ so that Eqs. (6), (8) and (9) can be related. These equations are then subject to the initial and boundary conditions:

$$P = P^o_{sys} = \text{constant}, \quad t = 0, \quad 0 < z < L \tag{10a}$$

$$P = P_{sys}(t), \quad z = L, \quad t > 0 \tag{10b}$$

$$dP/dz = 0, \quad z = 0, \quad t > 0 \tag{10c}$$

where P^o_{sys} is the initial coolant pressure at $t = 0$ and $P_{sys}(t)$ is the bulk system pressure (i.e., at the breached end of the rod). Equation (10c) follows from Eq. (9) where it is assumed that the velocity $u = 0$ at the intact end of the rod.

2.2 *Production and Loss Terms for the Transport Equations*

2.2.1 *Fission Gas Source Term*

A calculation of the fission gas source term q_1 is required for Eqs. (4a) and (4b). Mechanistic treatments have been developed to assess the distribution and release of fission gas from the solid fuel matrix by considering the combined effects of fission product generation, atomic migration, bubble nucleation and resolution, bubble migration and coalescence, channel formation on grain faces, interlinking on grain edges, microcracking and grain boundary sweeping.[13,16,17] For the current analysis, a model is required to predict the stable gas release from the fuel for out-of-pile conditions at high temperature. If the fuel is trace-irradiated, significant grain growth can occur during the high-temperature anneal under an oxidizing environment due to an enhanced uranium ion diffusivity in UO_{2+x}, which supplements intragranular diffusion as a means of delivering fission products to the grain boundaries.

However, for higher burnup specimens (i.e., typical of the CRL fuel samples), the grain growth mechanism is limited with a pinning of the grain boundaries by fission product bubbles.[13] Hence, a simple annealing diffusion model can be adopted in the current treatment to support the gap-transport analysis of the CRL experiments. This model, however, must account for the possibility of a changing fuel stoichiometry and, as such, a generalized Booth diffusion type model can be employed for the evaluation of q_1 where[14]

$$q_1 = \left(\frac{V}{S}\right)_{fuel} \frac{c^o_{Xe}}{h} \frac{df_{rel}}{dt} \tag{11}$$

Here $(V/S)_{fuel}$ is the volume-to-surface ratio of the fuel (= $a_f/2$ where a_f is the fuel pellet radius) and h is the radial gap thickness. The parameter c^o_{Xe} is the initial fission gas concentration in the fuel:

$$c^o_{Xe} = Y_{Xe+Kr} c_U \beta_f \tag{12}$$

where Y_{Xe+Kr} is the rare gas fission yield (= 0.25 atom fission^{-1}), c_U is the molar density of uranium in UO_2 (= 41 × 10^3 mol m^{-3}), and β_f is the burnup fraction (i.e., 1 at% burnup equals 9.5 GWd/tU). The fission gas release rate from the fuel (df_{rel}/dt) can be evaluated from the slope of the diffusional release fraction:[10]

$$f_{rel} = \begin{cases} 6\sqrt{\dfrac{\tau}{\pi}} - 3\tau & \text{for } \tau \le 0.155 \\ 1 - \dfrac{6}{\pi^2}\exp\left(-\pi^2\tau\right) & \text{for } \tau > 0.155 \end{cases} \tag{13}$$

where $D'(t) = D/a^2$, and D is the time-dependent fission gas diffusivity in the fuel grain of radius a. The parameter τ is a dimensionless variable:

$$\tau = \int_0^t D'(t)\, dt \tag{14}$$

which accounts for a time-dependent diffusivity where the start of the transient is assumed to occur at $\tau = 0$. A variable diffusivity results from changing temperature conditions $T(t)$ during the transient. In addition, due to a changing oxygen potential in the gap (see Section 2.3), a variable stoichiometry deviation $x(t)$ in the UO_{2+x} fuel also arises. The functional dependence of the fission gas diffusivity (in m^2 s^{-1}) on both temperature and non-stoichiometry is given by:[9,10]

$$D(x,T) = 7.6\times10^{-10}\exp\left\{-\frac{70000}{RT}\right\} + 2.22\times10^{-8}x^2\exp\left\{-\frac{40200}{RT}\right\} \tag{15}$$

where R is the ideal gas constant (= 1.99 cal mol^{-1} K^{-1}) and T is in K. The quantity of fission gas release q_1 into the gap will implicitly depend on the mole fraction distribution (which in turn determines the local oxygen potential and the subsequent fission gas solid-state diffusivity in the fuel matrix). Hence, an iteration will be required for solution of Eqs. (13) and (15) when feedback effects are considered.

The fuel exhibits structural defects like porosity that is not taken into account in the present model, where fission product trapping may in fact occur. To account for this effect, a simple scaling parameter ξ can be introduced. In addition, fuel cracking can also occur on temperature ramp up, resulting in a partial release of the grain boundary inventory, which is not explicitly treated for the diffusional release process of Eq. (13), so that an additional source release g_o must be considered. Consequently, the release fraction in Eq. (11) can be replaced by an overall release function F to account for these effects: [9]

$$F = (1 - g_o - \xi) f_{rel} + g_o \tag{16}$$

2.2.2 *Loss Terms Due to Fuel Rod Oxidation Processes*

The production rate of hydrogen and the loss rate of steam are equal to one another for a given chemical process. This result arises since the molar quantities of hydrogen and steam are balanced in each oxidation reaction for the Zircaloy and fuel:

$$Zr + 2H_2O \Leftrightarrow ZrO_2 + 2H_2 \tag{17a}$$

$$xH_2O + UO_2 \Leftrightarrow UO_{2+x} + xH_2 \tag{17b}$$

where x is the stoichiometry deviation in UO_{2+x}. The kinetics for these oxidative processes are detailed in the following sections.

2.2.2.1 Steam Loss Reaction Rate By Urania Oxidation.

The steam loss rate due to fuel oxidation is given by:[8]

$$r_2^{fuel\ ox} = \frac{c_U}{h}.\frac{dx}{dt} = \frac{c_U \left(P_{H_2O}\right)^{1/2} \alpha}{h}\left\{x_e - x(t)\right\} \tag{18}$$

where P_{H_2O} is the steam pressure (atm), α is a surface exchange coefficient (= 0.365 exp{-23500/T(K) m s^{-1}}), and x_e is the equilibrium stoichiometry deviation. Equation (18) can be integrated analytically, assuming that x_e is constant over a given time step Δt, for a calculation of $x(t)$.

The value of x_e in Eq. (18) is obtained from the Blackburn thermochemical model:[18]

$$\ln P_{O_2} = 2\ln\left(\frac{x_e(2+x_e)}{1-x_e}\right) + 108x_e^2 - \frac{32700}{T} + 9.92 \tag{19}$$

where $P_{O_2}(x)$ is calculated as shown in Section 2.3.

2.2.2.2 Steam Loss Reaction Rate By Internal Clad Oxidation

The steam loss rate for the internal Zircaloy oxidation process can be described by:

$$r_2^{clad\ ox} = \frac{\dot{w}_{tot}^{inside}}{h}. \tag{20}$$

The metal water reaction is mass transfer limited by the amount of steam which is available in the gap for consumption in the given time step Δt such that:

$$\dot{w}_{tot}^{inside} = \min\left(\dot{w}_{corr}, \dot{w}_c^{inside}\right) \tag{21}$$

where:

$$\dot{w}_c^{inside} = c_2 \frac{h}{\Delta t}. \tag{22}$$

Here $c_2 = y_2 c$ is the molar concentration of steam in a given control volume within the gap that decreases towards the intact end of the rod. This steam will react more rapidly with the cladding than with the fuel where equilibrium thermodynamics indicates that the free energy of formation of the oxide is lower for ZrO_2 than for UO_{2+x}.[11,14] Thus, in the model, any steam unconsumed in a given control volume will then become available for oxidization of the fuel. The time step Δt must be sufficiently small so as not to artificially limit these oxidation reactions.

The corrosion rate, $\dot{w}_{corr}$, can be estimated from parabolic rate theory where the mass of zirconium consumed per unit area per unit time (kg m^{-2} s^{-1}) by the steam reaction is:[19]

$$\dot{w}_{corr} = \frac{1}{M_{Zr}} \sqrt{\frac{k_w}{t}}. \tag{23}$$

Here M_{Zr} is the molecular weight of zirconium (= 0.091 kg mol^{-1}) and k_w is the parabolic rate constant:

$$k_w = k_{wo} \exp\left\{-\frac{Q_o}{RT}\right\} \tag{24}$$

where k_{wo} and Q_o are constants determined by various investigators as tabulated in Ref. 8 and detailed in Refs. 20 to 23. The Zircaloy oxidation reaction will cease when the total clad thickness is consumed. The parabolic model of Eq. (23) has been used to describe the Zircaloy oxidation process in the current analysis since its numerical implementation is quite straightforward as compared to a more complex moving-boundary diffusion treatment as detailed in Ref. 24 (see Section 3.4.1). The parabolic model is only strictly valid for a semi-infinite medium however, under isothermal conditions (i.e., relevant to the CRL anneal tests), both models yield identical kinetics until a small thickness of Zircaloy is left after which the diffusion model indicates a slightly accelerated behaviour. This difference between the two models does not give rise to a significant variation in the hydrogen generation prediction as observed in annealing experiments at the Oak Ridge National Laboratory.[25]

2.3 *Oxygen Potential in the Gap*

The oxygen potential along the gap as a function of time can be obtained from the mole fractions solutions (i.e., partial pressures) of the gap transport equations in Section 2.1. As previously mentioned, however, there is a feedback effect where the source term of fission gas (q_1) in Section 2.2.1 actually depends on the state of fuel oxidation which, in turn, is affected by the oxygen potential.[10]

The oxygen potential for an ideal gas mixture in the gap consisting of Xe, H_2O and H_2 can be evaluated following the methodology of Ref. 9. For the H_2O decomposition reaction

$$H_2O \overset{K_{H_2O}}{\Leftrightarrow} H_2 + \tfrac{1}{2} O_2 \tag{25}$$

the equilibrium constant is

$$K_{H_2O} = \frac{P_{H_2}\sqrt{P_{O_2}}}{P_{H_2O}} = \exp\left\{0.9794 \ln T - 1.1125 - \frac{28820}{T}\right\} \tag{26}$$

The oxygen partial pressure, P_{O_2} (in atm), can therefore be evaluated at equilibrium on solving the following cubic equation, which results from mass balance considerations for the H and O in the gas mixture before and after steam dissociation:

$$4\left(P_{O_2}\right)^3 + 4\left[P^o_{H_2} - K^2_{H_2O}\right]\left(P_{O_2}\right)^2 + \left[\left(P^o_{H_2}\right)^2 + 4P^o_{H_2O}K^2_{H_2O}\right]P_{O_2} - \left[\left(P^o_{H_2O}\right)^2 K^2_{H_2O}\right] = 0 \tag{27}$$

Here the superscript "o" refers to the initial partial pressure quantities derived from the solution of the gap transport equations in Section 2.1. Equation (27) can be solved either numerically or analytically.

2.4 Boundary Conditions In the Bulk Coolant

The mole fraction of steam in the bulk coolant at the defect site (e.g., $y_2^c(t)$ in Eq. (7c)) is a boundary condition, which must be known for solution of the gap transport equations. Although steam is initially the main component in the RCS at the start of the transient, hydrogen will also be generated as a consequence of external clad oxidation during the high-temperature transient.

The mole fraction distributions in the RCS can be derived from the continuity equation:[8]

$$\frac{\partial\left(c^c\, y^c_{H_2O}\right)}{\partial t} = -\frac{Q}{S_c}\frac{\partial y^c_{H_2O}}{\partial z} - r^{\text{ext clad ox}}_{H_2O}, \tag{28}$$

where Q (mol s^{-1}) is the total molar gas flow rate of the bulk coolant through a cross-sectional flow area S_c (m^2). Here c^c is the total molar gas concentration in the RCS such that:

$$c^c = \frac{P_{sys}(t)}{RT_{sys}(t)}. \tag{29}$$

The parameter $r^{\text{ext clad ox}}_{H_2O}$ (mol m^{-3} s^{-1}) in Eq. (28) accounts for steam losses due to external clad oxidation

$$r^{\text{ext clad ox}}_{H_2O} = \left(\frac{\pi d}{S_c}\right)\dot{w}^{ext}_{tot}, \tag{30}$$

where d is the fuel rod diameter (m). Equation (30) must account for mass transfer limitations through the boundary layer on the outside cladding surface such that:[26,27]

$$\dot{w}^{ext}_{tot} = \min\left(\dot{w}_{corr}, \dot{w}^{ext}_{MT}\right), \tag{31}$$

where $\dot{w}_{corr}$ is again evaluated in accordance with the parabolic kinetics of Eq. (23) and

$$\dot{w}^{ext}_{MT} = k_g\, y^c_{H_2O}. \tag{32}$$

Here the mass transfer coefficient k_g (mol m^{-2} s^{-1}) is obtained from a heat-mass transfer analogy:[10,11,15]

$$Nu_{ij} = \frac{k_g D_e}{cD_{ij}} \approx 4, \tag{33}$$

where Nu_{ij} is the Nusselt number for mass transfer (which equals 4 for laminar flow), D_e is the equivalent diameter that equals the channel diameter minus the fuel rod diameter, and D_{ij} is the diffusion coefficient for the H_2O-H_2 binary mixture.

Thus, neglecting any inert gas in the bulk coolant, the hydrogen and steam molar distributions in the RCS follow on solution of Eqs. (28) to (33). Equation (28) is subject to the following initial and boundary conditions:

$$\begin{aligned} y^c_{H_2O} &= y^o_{H_2O}, \quad t = 0, \quad 0 < z < L \\ y^c_{H_2O} &= y^{\text{input}}_{H_2O}, \quad z = 0, \quad t > 0 \end{aligned} \tag{34}$$

where $y^{o}_{H_2O}$ is the initial mole fraction for steam in the bulk coolant and $y^{\text{input}}_{H_2O}$ is the input mole fraction of steam in the bulk coolant at $z = 0$. The corresponding distribution for hydrogen is determined from the mass balance relation $y^{c}_{H_2} = 1 - y^{c}_{H_2O}$ (neglecting any fission gas in the RCS).

The parabolic model of Eq. (23) is only strictly valid for oxidizing conditions. In contrast to a moving-boundary diffusion model, the parabolic model cannot account for any physical shrinkage of the oxide scale due to its dissolution in the remaining metal during steam starvation.[27] Moreover, in the event that the oxide scale completely disappears, hydrogen can also rapidly saturate the metal, resulting in a removal of hydrogen from the bulk gas flow.[27] These effects are not considered in the current treatment.

3. NUMERICAL IMPLEMENTATION

3.1 *Numerical Discretization of the Gap Transport Equation*

Equations (4a) and (4b) can be discretized using a finite-difference scheme over an axial mesh as illustrated in Fig. 1. For the first derivative, the following finite-difference approximation is used (where the discretization index is in brackets):

$$\frac{\partial f}{\partial z} = \frac{f(i+1) - f(i-1)}{\Delta z(i-1) + \Delta z(i)} \tag{35}$$

Thus for calculation of the derivatives in Eqs. (4a) and (4b), the first-order derivatives are replaced by the two lateral finite-difference forms:

$$cD\frac{\partial f}{\partial z} = \begin{cases} c^{-}(i)D^{-}(i)\dfrac{f(i) - f(i-1)}{\Delta z(i-1)} & \textit{left lateral first derivative} \\ c^{+}(i)D^{+}(i)\dfrac{f(i+1) - f(i)}{\Delta z(i)} & \textit{right lateral first derivative.} \end{cases} \tag{36}$$

These lateral derivatives are estimated at the midpoints of the mesh intervals "(*i*-1)" and "*i*" respectively in Fig. 1. The second derivative in Eq. (4) is then replaced by the finite-difference equivalent:

$$\frac{\partial}{\partial z}\left[cD\frac{\partial f}{\partial z}\right] = \frac{1}{(ZOT - ZIN)}\left\{\frac{c^{-}(i)D^{-}(i)}{\Delta z(i-1)}f(i-1) + \frac{c^{+}(i)D^{+}(i)}{\Delta z(i)}f(i+1) - \left[\frac{c^{-}(i)D^{-}(i)}{\Delta z(i-1)} + \frac{c^{+}(i)D^{+}(i)}{\Delta z_i}\right]f(i)\right\} \tag{37}$$

Here:

$$ZOT = \frac{1}{2}[z(i) + z(i+1)], \qquad ZIN = \frac{1}{2}[z(i-1) + z(i)] \quad \text{and} \quad ZOTN = ZOT - ZIN \tag{38a}$$

and the interval-effective diffusivities and interval-average molar concentrations are defined by:

$$D^{-}(i) = \frac{2D(i-1)D(i)}{D(i-1) + D(i)} \qquad D^{+}(i) = \frac{2D(i)D(i+1)}{D(i) + D(i+1)} \tag{38b}$$

$$c^{-}(i) = \frac{c(i-1) + c(i)}{2} \qquad c^{+}(i) = \frac{c(i) + c(i+1)}{2}$$

The following notation can be further used to define the coefficients of the discretized equations:

$$a'(i) = \frac{c^{-}(i)D^{-}(i)}{ZOTN\Delta z(i-1)}, \quad c'(i) = \frac{c^{+}(i)D^{+}(i)}{ZOTN\Delta z(i)}, \quad b'(i) = a'(i) + c'(i) \tag{39a}$$

and

$$a''(i) = \left[a'(i) + \frac{N_T}{\Delta z(i-1) + \Delta z(i)} \right], \quad c''(i) = \left[c'(i) - \frac{N_T}{\Delta z(i-1) + \Delta z(i)} \right], \quad b''(i) = \left[b'(i) + q_1(i) \right] \tag{39b}$$

where $q_1(i)$ corresponds to the xenon source term at mesh point i. Thus, using these definitions, Eqs. (4a) and (4b) can be discretized, respectively, where on considering the multicomponent indices that arise from the diffusion coefficients:

$$-\frac{c(i)}{\Delta t} y_1^o(i) - q_1(i) = \{a_{11}''(i) y_1^n(i-1) - [b_{11}''(i) + \frac{c(i)}{\Delta t}] y_1^n(i) + c_{11}''(i) y_1^n(i+1)\} + \{a_{12}'(i) y_2^n(i-1) - b_{12}'(i) y_2^n(i) + c_{12}'(i) y_2^n(i+1)\} \tag{40a}$$

$$-\frac{c(i)}{\Delta t} y_2^o(i) + r(i) = \{a_{22}''(i) y_2^n(i-1) - [b_{22}''(i) + \frac{c(i)}{\Delta t}] y_2^n(i) + c_{22}''(i) y_2^n(i+1)\} + \{a_{21}'(i) y_1^n(i-1) - b_{21}'(i) y_1^n(i) + c_{21}'(i) y_1^n(i+1)\} \tag{40b}$$

where $r(i) = r_2^{clad\ ox}(z_i, t) - r_2^{fuel\ ox}(z_i, t)$. The y_1^o and y_2^o parameters in Eqs. (40a) and (40b) correspond to the previous time-step values.

At the intact end of the fuel pin (i.e., $i = 0$) (see Fig. 1), the boundary condition in Eq. (7b) is implemented by assuming a virtual point at $i = -1$ and equating its value to that of $i = 1$ for a reflective condition. Also, the second term on the right hand side in Eqs. (4a) and (4b) is zero at $i = 0$ for the condition in Eq. (7b). Due to the symmetry of the parameters in Eq. (39) around $i = 0$, it follows that $a'(0) = c'(0)$ in Eq. (39a) and therefore $b'(0) = 2c(0)$. Moreover, the double-primed coefficients for a and c in Eq. (39b) reduce to the primed ones in Eq. (39a) since there is no flow at $i = 0$. The coefficient $ZOTN$ in Eq. (38a) is also equal to Δz_1.

The boundary conditions in Eqs. (7c) at the breached end (i.e., $i = N+1$) are implemented so that the first term on the left hand side of Eqs. (40a) and (40b) can be moved to the left hand side since these quantities are now known.

3.2 *Solution of the Linear System of Equations*

The discretized equations in Eqs. (40a) and (40b), constitute a linear system which can be written in matrix form:

$$\mathbf{AY} = \mathbf{B} \tag{41a}$$

or alternatively

$$\begin{bmatrix} AL1 & AR1 \\ AL2 & AR2 \end{bmatrix} \begin{bmatrix} y_1^n(1) \\ . \\ . \\ y_1^n(N) \\ y_2^n(1) \\ . \\ y_2^n(N \end{bmatrix} = \begin{bmatrix} -\frac{c(1)}{\Delta t} y_1^o(1) - q_1(1) \\ . \\ . \\ -\frac{c(N)}{\Delta t} y_1^o(N) - q_1(N) \\ -\frac{c(1)}{\Delta t} y_2^o(1) + r(1) \\ . \\ . \\ -\frac{c(N)}{\Delta t} y_2^o(N) + r(N) \end{bmatrix} \tag{41b}$$

Here the matrix **A** is composed of four tri-diagonal N x N blocks called $AL1$, $AL2$ for the y_1 part and $AR1$, $AR2$ for the y_2 part, where the sub-matrices have the form:

$$AL1 = \begin{matrix} -b_{11}''(1) - \frac{c(1)}{\Delta t} & c_{11}''(1) & 0 & 0 \\ a_{11}''(2) & -b_{11}''(2) - \frac{c(2)}{\Delta t} & c_{11}''(2) & 0 \\ 0 & a_{11}''(3) & -b_{11}''(3) - \frac{c(3)}{\Delta t} & c_{11}''(3) \\ 0 & 0 & .... & . \\ & & \ddots & \end{matrix} \quad AR1 = \begin{matrix} -b_{12}'(1) & c_{12}'(1) & 0 & 0 \\ a_{12}'(2) & -b_{12}'(2) & c_{12}'(2) & 0 \\ 0 & a_{12}'(3) & -b_{12}'(3) & c_{12}'(3) \\ 0 & 0 & .... & . \\ & & \ddots & \end{matrix}$$

$$AL2 = \begin{matrix} -b_{21}'(1) & c_{21}'(1) & 0 & 0 \\ a_{21}'(2) & -b_{21}'(2) & c_{21}'(2) & 0 \\ 0 & a_{21}'(3) & -b_{21}'(3) & c_{21}'(3) \\ 0 & 0 & .... & . \\ & & \ddots & \end{matrix} \quad AR2 = \begin{matrix} -b_{22}''(1) - \frac{c(1)}{\Delta t} & c_{22}''(1) & 0 & 0 \\ a_{22}''(2) & -b_{22}''(2) - \frac{c(2)}{\Delta t} & c_{22}''(2) & 0 \\ 0 & a_{22}''(3) & -b_{22}''(3) - \frac{c(3)}{\Delta t} & c_{22}''(3) \\ 0 & 0 & .... & . \\ & & \ddots & \end{matrix} \tag{42}$$

The solution procedure is an adaptation of the Gauss-Jordan reduction method by taking advantage of a banded structure to reduce the computational requirements. At the end of this procedure, the upper left sub-matrix is diagonalized and the lower left sub-matrix is reduced to zero, while the upper right sub-matrix is full but the lower right sub-matrix is brought to a triangular form with the lower part zeroed. This permits a back-substitution process to be performed, first for y_2:

$$y_2(i) = [tb(i) - \sum_{j=i+1}^{N} ar2(i,j) y_2(j)] / ar2(i,i) \tag{43a}$$

where $ar2$ denotes the elements of the $AR2$ matrix and tb stands for the bottom free term corresponding to y_2.
For the computation of y_1, all values of y_2 will be used since $AR1$ is full at the end of the reduction process**:**

$$y_1(i) = [tu(i) - \sum_{j=1}^{N} ar1(i,j) y_2(j)] / al1(i,i) \tag{43b}$$

and $ar1$ and $ar2$ correspond to the elements of the $AR1$ and $AR2$ matrices, respectively.

3.3 Solution of Gas Bulk -Flow Equations

It is traditional to solve gas flow problems with a CV (Control-Volume) technique on a staggered mesh for the continuity equation (Eq. (6)) and the momentum equation (Eq. (9)). A fully implicit scheme is employed for improved stability. The CV grid is shown in Figure 1, with an overlaid finite-difference mesh, which coincides with the CV midpoints. The following parameters are defined at the CV midpoints: the pressure, molar concentration, temperature and source/loss terms, while the molar flux is defined at the rightward side of a given CV. The CV equations are obtained by integrating the differential equations over a CV and applying the mean-value theorem for scalar expressions, and the Stoke's theorem for expressions which involve any gradients. The result of applying this procedure to Eqs. (6) and (9) is:

$$(c_i^n - c_i^o)/\Delta t + [(N_T)_i^n - (N_T)_{i-1}^n]/\Delta z_i = q_i \tag{44}$$

where, i, indexes the CV's, while the superscripts "n" and "o" correspond to "new" and "old" values, respectively. Moving the old values to the RHS, Eq. (44) can be re-written as

$$c_i^n + [(N_T)_i^n - (N_T)_{i-1}^n]\Delta t/\Delta z_i = q_i \Delta t + c_i^o \tag{45}$$

The momentum equation (Eq.(9)) is discretized by integrating it around the interface between CV "(i)" and CV "(i+1)" and taking half of the corresponding CV's to obtain

$$(N_T)_i^n + \alpha_i^o \frac{P_{i+1}^n - P_i^n}{\Delta z_{i,i+1}} = 0 \tag{46}$$

Here $\alpha_i^o = h^2 c_i^o/(12\mu_i)$, and $\Delta z_{i,i+1}$ represents the distance between the midpoints of CV's "(i)" and "(i+1)" (which is identical to the spatial step quantity $\Delta z(i)$ in the finite-difference mesh). Equation (46) can be used to eliminate the molar fluxes (N_T) in Eq. (45). Furthermore, using the equation of state in Eq. (8), Eq. (45) can be written in terms of the gas pressure P such that:

$$a_i P_{i-1}^n + b_i P_i^n + c_i P_{i+1}^n = d_i \tag{47a}$$

where

$$\begin{aligned} a_i &= \alpha_{i-1}\Delta t/(\Delta z_i \Delta z_{i-1,i}), \\ c_i &= \alpha_i \Delta t/(\Delta z_i \Delta z_{i,i+1}), \\ b_i &= -a_i - c_i - 1/(RT_i), \\ d_i &= -q_i \Delta t - c_i^o \end{aligned} \tag{47b}$$

For the intact end of the fuel pin (i = 0), the molar flux is zero so that a_0 is zero in Eq. (47a). At the breached end, P_{N+1} is equal to the given system pressure as detailed in Eq. (10b). The system of equations in Eq.(47) is a tri-diagonal system, which can be directly solved by an adaptation of the Gauss-Jordan elimination method similar to that used in Section 3 for solution of the transport equations. Thus, with back-substitution:

$$P_i = d_i / b_i \tag{48}$$

Once the new values of gas pressure along the fuel pin are determined with the solution of Eq. (47), the molar fluxes N_T needed for the gap transport equations, can be calculated via Eq. (46).

3.4 Oxidation Treatment

3.4.1 Zirconium Oxidation

For the numerical implementation, the parabolic rate law of Eq. (23) can be written as:[28]

$$\dot{w}_{corr} = \frac{dw(t)}{dt} = \frac{\sqrt{w^2(t) + k_w \Delta t} - w(t)}{\Delta t} \tag{49}$$

For the external zirconium oxidation reaction, steady state conditions can be assumed, i.e., $\partial\left(c^c y^c_{H_2O}\right)/\partial t = 0,$ since the storage capacity of gas in the cell is much less than the total quantity of steam fed to the cell for the normal time duration of a typical experiment or accident.[27] As such, Eq. (28) can be directly integrated over the cell distance Δz and if $r^{\text{ext clad ox}}_{H_2O}$ is constant over Δz[27]

$$y^c_{H_2O}(z + dz) = y^c_{H_2O}(z) - \left(\frac{A_c}{Q}\right)\dot{w}^{ext}_{tot} \tag{50}$$

where Eq. (30) has been used in this discretization. Ac (= πd Δz) is the surface area of the clad in the given cell volume. Thus, the steam distribution in the reactor coolant system can be given by the marching numerical solution of Eq. (50).

3.*4 Fuel Oxidation*

Equation (27) is usually solved numerically for the oxygen mole fraction β (where $P_{O_2} = \beta/2$). However, when the hydrogen concentration is very small, the numerical solution becomes unstable and the cubic equation can then be solved analytically. The final partial pressures after dissociation follow as:

$$\begin{aligned} p_{H_2O} &= p^0_{H_2O} - \beta \\ p_{H_2} &= p^0_{H_2} + \beta \end{aligned} \tag{51}$$

where the terms containing the superscript "o" correspond to the partial pressure solution of the gap transport equation prior to dissociation. The oxygen potential in the gap follows from the standard definition:

$$\Delta G_{O_2} = RT \ln(P_{O_2}) \tag{52}$$

By equating the oxygen potential in the gap to that in the fuel, Eq. (19) can now be solved. Thus, with a knowledge of the oxygen partial pressure in the gap, $P_{O_2} = \beta/2$, Eq. (19), when written in the form $f(x_e) = 0$, can be solved by a standard Newton-Raphson numerical technique for x_e.

4. MODEL ANALYSIS

The transport model was applied to annealing experiments performed at the Chalk River Laboratories (CRL). A description of the experiments is given in Section 4.1 and their simulation is detailed in Section 4.2. Section 4.3 provides an interpretation of the fuel-rod oxidation and fission product release behaviour observed in these experiments based on a model analysis.

4.1 Experimental Description

In the CRL experiments, short-length "mini-elements" were fabricated by cutting a section of a spent Candu-type fuel element and adding loose-fitting end caps onto the cladded fuel segment. Each fuel specimen was introduced into a flowing mixture of argon/2%H_2 (400 mL/min at STP) and ramped to a given temperature plateau as detailed in Table 1. After the temperature-plateau had been reached, the fuel was exposed to an oxidizing mixture of steam (60 g/h) and argon (100mL/min at STP). The details of the experiments are summarized in Table 1.[9]

Post-test metallography was performed on each of the three fuel specimens. The post-test micrographs of HCE2-CM1 sample (1915 K) is shown in Fig. 2. A piece of one end-cap is missing, but this probably occurred during handling after the test. Single-sided oxidation of the sheath and significant UO_2-Zircaloy interaction was observed. The gap had opened up in some areas by distortion of one side of the sheath, resulting in a more open pathway for atmosphere exchange down the length of the mini-element. In experiment HCE2 CM2 (1628 K), the oxidized sheath was fragmented during handling and cracks in the oxidized sheath during the test cannot be ruled out. In experiment HCE2 CM6 (1768 K), a segment of the sheath and part of an end-cap were examined. In these latter two tests, double-sided oxidation had occurred, implying a significant atmosphere-exchange even before the completion of sheath oxidation.

The precise size of the radial gap in these experiments at temperature is unknown from the post-test examination due to differences in the thermal expansion of the Zircaloy clad and UO_2 fuel. The fuel will also swell due to expansion of fission gas in the fuel matrix porosity. On oxidation of the cladding, there is also an increase in volume (with a Pilling-Bedworth ratio of 1.56 for zirconium dioxide). For example, on annealing a cladded sample to 1870 K in a furnace, the area of the UO_2 expands by 3.7% while the area encompassed by the Zircaloy sheath expands by between 1.6 and 2.8%.[29] Prior to the annealing, the mini-elements exhibit a cracked-fuel structure, as typically shown in Fig. 3. Although these cracks could close up by the difference in thermal expansion, the cracks will be resistant to closure by compression of the sheath because of possible rearrangement of the fragments,[30] and the fact that the Zircaloy (at elevated temperatures) is soft enough that it will deform before it can apply a significant compressive force.[29] Residual cracks will also exist in the fuel element at temperature when the thermoelastic stress components exceed the fracture strength of the fuel in tension. This cracking can also provide a limited network (in addition to that of the gap) for atmosphere exchange throughout the mini-element. Such cracking, however, is not typical of an in-reactor event since cracking does not occur in the plastic zone of the fuel.

4.2 Experiment Simulation

For application of the one-dimensional model, it is implicitly assumed that the loose-fitting end caps do not offer any restriction to the atmospheric exchange. Moreover, with the model representation of Fig. 1 (where steam can only enter at the downstream end of a defective rod), the experimental specimens can be simulated by considering a path length of half their actual length. This type of analysis follows from symmetry arguments since the same reflexive condition (i.e., at the intact end of the rod in Fig. 1) will result at the centre of the fuel rod when it is breached at both ends.[3] Thus, as shown in Ref. 3, a rod with a breach at both ends can be simulated as two half-length rods with a breach at only one end. This symmetry argument can also be extended to many equally-spaced breached sites along the entire cladding length.[3]

For the current simulation of the CRL experiments, only one-half of the rod was therefore considered for the model of Fig.1 since the fuel specimens had loose-fitting end caps at both ends. This treatment is only approximate since it does not properly account for the presence of pure steam as a boundary condition at the upstream end but rather assumes the given steam/hydrogen mixture at the downstream end which results from external clad oxidation in the RCS along the simulated length. However, once external-clad oxidation is complete, the current representation is directly applicable (with a uniform steam boundary condition in the RCS).

As previously mentioned, in a high-temperature steam atmosphere, the zirconium cladding oxidizes where the resultant oxide occupies a larger volume than the metal. This volume change can cause additional stress in the brittle oxide, leading to possible cracking and fragmentation as indicated in the metallographic analysis (see Section 4.1). Initially, any thermal stress should not cause cracking because the Zircaloy metal is ductile, however, later in the oxidation process, cracks may form in the brittle oxide layer. Thus, to account for this possibility of enhanced

atmospheric exchange, an empirical cracking model is introduced by simply reducing the path length for gap transport, i.e., by considering a number of shorter-length segments in accordance with the symmetry arguments of Ref. 3. Experimental simulations were carried out for the three short-length mini-elements CM2, CM6 and CM1, with an outer diameter of 13.11 mm for the experiments at temperatures of 1628 K, 1768 K and 1915 K, respectively. The temperatures were measured using a Type T thermocouple within a few millimeters of the sample and were known within a relative error of 1.5%. An input RCS steam mole fraction of $y_{H_2O}^{\text{input}} = 1$ (with an external gas flow rate of $Q = 9 \times 10^{-4}$ mol s^{-1}) at atmospheric pressure (P_{sys} = 1 atm) was used. The initial mole fractions for the gap atmosphere were taken as $y_1^o = 0$ (xenon), $y_2^o = 1$ (steam) and $y_3^o = 0$ (hydrogen).

The mini-elements were composed of standard CANDU fuel pellets with a diameter 12.15 mm. The mini-elements also had a cladding thickness of 0.43 mm and an overall length of 9 mm (CM2), 11 mm (CM6) and 10 mm (CM1). An internal gap size of 20 μm was assumed in all of the analysis. This latter input parameter represents the largest uncertainty in the given analysis (see Section 4.3). A diametral gap of D_e = 1.2 cm for the test rig setup was used in the mass transfer calculation of Eq. (33). In addition, the intermolecular parameters for hydrogen and steam for the binary diffusivity in Eq. (33), and the coefficients of Urbanic and Heidrick for the parabolic rate constant in Eq. (24), are obtained from previous work.[9] For the fuel oxidation model, a surface-to-volume (S/V) ratio of three times the geometric value (see Table 2) was used to account for surface roughness and fuel cracking effects as suggested in Ref. 9.

This simulation was performed with 30 mesh points along the length of the element, yielding a spatial step size Δz of 0.18 mm. With the assumption of cracking, the spatial step size was reduced to 0.02 mm. The time step size Δt was varied between 0.1 and 0.5 ms, where a smaller step size was required for stability at high temperature with the cracked-clad model.

4.3 Analysis of Numerical Results

The predicted fractional release is presented in Fig. 4(a). These results can be compared to the experimental measurements of the volatile cesium release obtained at the CRL. The relative uncertainty for the measured cesium release fractions was ~1% (for one standard deviation). Prior to complete clad oxidation, the release kinetics are in reasonable agreement but are underpredicted after this time. A sensitivity analysis of the model was further performed by increasing the size of the radial gap ten-fold. Thus, even with the largest possible gap width of 220μm (as observed in the metallographic examination at room temperature), the release is still considerably underpredicted for the low-temperature experiment. Moreover, this large gap size also did not provide for the correct timing for the completion of clad oxidation as well as for the effect of single or double-sided oxidation as discussed below. As mentioned, the geometry of the mini-element is not exactly reproduced, where (pure) steam entry at the upstream end could enhance the local fuel oxidation process (while external clad oxidation is occurring). However, this effect would not be significant due to continued hydrogen production from (internal) clad oxidation, which would lower the oxygen potential and restrict any fuel oxidation. This scenario was in fact exploited in the analysis of Ref. 14 where it was assumed that the defect site acts as a source of hydrogen production (due to clad oxidation). Indeed, the model is able to predict reasonably well the time that the fission product release (and hence fuel oxidation) starts to take off in all three experiments following complete clad oxidation. On the other hand, after this time, not enough steam is able to enter into the fuel rod at the breach location. Thus greater atmospheric exchange must be occurring, indicating increased oxygen transport.

One possibility for increased oxygen transport is the presence of a cracked oxide layer. This type of effect can be modelled with a reduced gap-transport length following clad oxidation when the oxide is most susceptible to cracking. With the lack of a mechanistic cracking model for this stochastic effect, one can invoke an empirical approach by assuming symmetrically-spaced cracks for the mini-elements in the simulation. Thus, in order to match the observed release behaviour, the following number of cracks are required: two cracks for CM2 at 1915 K (i.e., path length of 1.7mm), five cracks for CM6 at 1768 K (i.e., path length of 0.9 mm), and eight cracks for CM1 at 1628 K (i.e., path length of 0.5mm). As seen in Fig. 4(b), the cracked model is now able to reproduce the fractional release behaviour much better.

Since cracking is not assumed to occur until after complete clad oxidation, the non-cracked and cracked models yield identical results up to this point. In fact, both of these models are able to predict the observed Zircaloy oxidation behaviour including whether single-sided or double-sided oxidation had occurred in accordance with the metallographic examination of Section 4.1 (see Fig. 5). For the high-temperature case, the model predicts essentially single-sided oxidation (see Fig. 5(a)). In this case, the clad-oxidation process proceeds so quickly that there is little time for steam penetration, particularly with an enhanced fission gas release (at the elevated temperature) which retards such penetration. On the other hand, for the two lower temperature tests, more steam penetration is predicted to occur (see Fig. 5(b)), which results in the observed double-sided oxidation behaviour. It is interesting to note that a greater number of cracks are needed to reproduce the observed results in those experiments where double-sided oxidation had occurred. As previously mentioned, the model is also able to predict in Fig. 4 when the fission product release will take off at the end of the Zircaloy-oxidation stage; i.e., at this time, the oxygen potential in the gap increases since hydrogen is no longer being produced from metal-water reaction.

The model describes the hydrogen/steam distribution in the bulk coolant system, as well as in the fuel-to-clad gap, over the length of the fuel segment. This calculation yields a comparison of the corresponding oxygen potentials in the RCS and gap, as shown in Fig. 6(a) at the end of clad oxidation phase (which is appropriate to both models) and in Fig. 6(b) for a cracked rod at the end of the low-temperature experiment. Clearly, the oxygen potential within the gap is less than that in the bulk coolant, which can be principally attributed to a local hydrogen production from urania oxidation. As expected, with completion of fuel oxidation, the oxygen potential in the gap approaches that of the bulk coolant (see Fig. 6(b)).

Figures 7(a) and (b) show the average stochiometry deviation (x), equilibrium stochiometry deviation (x_e) and thickness of oxidized zirconium (at three different positions along the element length), as predicted by the model as a function of time, for both the low and high temperature experiments. As discussed earlier and depicted in the figure, the fuel does not start to oxidize until the clad is fully oxidized. Both the clad and fuel oxidation processes are faster with increasing temperature. The end-of-test stochiometry deviations for the three experiments are in reasonable agreement with estimated values derived from the weight gain (see Table 2), although these estimates are subject to a large uncertainty that cannot be specifically quantified. In particular, a difference in the upstream and downstream oxygen sensor data provide an integral measurement of oxidation of the clad and fuel. Thus, with a determination of the total oxygen consumption for the mini-element from the oxygen sensor data, and using the calculated weight gain for a completely oxidized clad, an estimate of the fuel weight gain (and hence stoichiometry deviation) can be deduced as reported in Table 2.

In summary, the results of the fully-mechanistic transport calculation, derived from a solution of the Stefan-Maxwell equations for the multi-component gap mixture, suggest that there must be an enhanced oxygen exchange occurring following completion of clad oxidation. In particular, initially with steam reaction, the zirconium forms an oxide in which oxygen-ion diffusion predominates over cation diffusion where simple diffusion results in scale formation at the metal-scale interface. However, a large increase in volume due to the Pilling-Bedworth ratio induces severe tensile stress into the scale so that fracture occurs in the brittle ZrO_2 layer which becomes porous on a microscopic scale and cracked on a macroscopic scale.[31] Consequently, following complete clad oxidation, oxygen molecules can diffuse in the gas phase filling the voids which offers much less resistance for oxygen transport.[31] To account for this enhanced transport, a cracked-oxide model was therefore adopted (i.e., in order to predict the enhanced cesium release kinetics). If the oxide layer were completely intact and protective, oxygen transport through the layer would be more restrictive and could only occur by solid state diffusion. In the next section (Section 5), it is further investigated by atomistic simulation if the oxidized cladding without cracks can act as a physical barrier to hydrogen and oxygen diffusion.

5. ATOMISTIC MODELLING

Detailed studies of hydrogen and oxygen diffusion through zirconia clad were carried out using a molecular-dynamics (MD) approach, with the interactions between atoms represented by a Modified Embedded Atom Method (MEAM) [32]. The MEAM is an empirical extension of the embedded atom method (EAM) that includes angular forces and is therefore suitable to study nonmetallic systems like oxides.

5.1 Modified Embedded Atom Potentials for the Zr-O-H System

The MEAM potentials for Zr-O-H system has been developed and the details will be described in our future publication. The estimated parameters[32] presented in Table 2 predict the lattice constant and cohesive energy of cubic ZrO_2 (the unit cell shown in Fig. 8) in excellent agreement with experiment. The structure of ZrH_2 does not remain tetragonal but rather transforms to a cubic structure with the same volume as the tetragonal phase. Additionally, the simulation is able to produce the correct formation energy, bond distances and angles for H_2O.

5.2 Molecular Dynamics Simulation

The MD simulations were performed for a slab of ZrO_2 with 288 atoms (see Fig. 9) and periodic boundary conditions. The (110) surface has been chosen since it is a more stochiometric surface than for example the (100) surface. The current simulation is performed in order to investigate if the oxidized cladding can act as a physical barrier to either hydrogen or oxygen diffusion at the temperature of the anneal experiment (i.e. 1700 K). The oxygen or hydrogen atoms are initially positioned outside of the slab at a distance that is shorter than the radius of the cutoff potential. The current simulation indicates that while oxygen diffuses into the bulk through the (110) surface, another oxygen atoms leaves the same surface of the bulk slab (Fig. 10). Hydrogen does not diffuse into the bulk slab since it becomes trapped by oxygen atoms on the surface. Occasionally, the hydrogen atom is kicked out from the surface and travels through the vacuum to the next available surface due to the periodic boundary condition or it can travel along the surface. Fig. 11 shows the results of the simulation for hydrogen after 50 psec, using a small time-step of $3x10^{-6}$ psec (i.e., a small time-step is required for an atom with a very small mass).

To obtain quantitative information about diffusion, mean-square displacements were first calculated:

$$< r^2(t) >=<|[r(t+t_o)-r(t_o)]^2|>_{t_o} \tag{53}$$

where the average is taken over all possible initial times t_o. The diffusion constants D from the Einstein relation can then be determined:

$$D = \lim_{t\to\infty} \frac{< r^2(t) >}{2dt} \tag{54}$$

where d is dimensionality of space (i.e., $d = 3$ for bulk diffusion). For a maximum time equal to 5000 psec (with a time-step of $5x10^{-4}$ psec), the diffusion constant is estimated as $5x10^{-9}m^2/s$, where the component perpendicular to the surface is equal to $4x10^{-13}m^2/s$. Thus, the current analysis suggests that for pure zirconia (i.e., without defects or impurities) oxygen diffusion occurs on the (110) surface mainly by surface diffusion.

A cluster of 324 atoms has been further created to study the bulk diffusion in defect-free zirconia. In this case, the diffusion constant of oxygen was estimated as $6x10^{-14}m^2/s$. Since this value is much less than that experimentally measured ($D = 4x10^{-9}m^2/s$ at 1700K),[33] diffusion must therefore be taking place through perhaps surface cracks, other planar defects or vacancies created by impurities.

5.3 Electrons Density and Hydrogen Diffusion

It is interesting that hydrogen, which diffuses easily in metals, is unable to diffuse into ZrO_2. The trapping of hydrogen in the presence of oxygen can be understood in terms of the change in electron density as the zirconium is oxidized. The electronic-structure calculations were performed (at temperature of 0 K) using a tight-binding linear muffin-tin orbital atomic-sphere-approximation.[34] The electron density of ZrO_2 was calculated for a (100) plane of a unit cell in the middle between a plane containing zirconium and one containing oxygen as indicated on Fig. 8. The same plane was chosen for the electron density calculations in pure zirconium.

The electron densities for zirconium and zirconia are shown on Figs. 12 (a) and (b). It can be seen that the electron densities in metallic zirconium are evenly distributed between 0.02 and 0.05 $Bohr^{-3}$ whereas, in zirconia, electrons are shifted towards oxygen with minimum and maximum densities of 0.006 and 0.16 $Bohr^{-3}$, respectively. Interestingly, as shown by Norskov,[35] the hydrogen energy is strongly dependent on the electron density within which it is embedded. Thus, it can be easily seen that hydrogen can become trapped in zirconia at electron densities

where its energy is at a minimum (and where it is surrounded by a high energy barrier created by high electron densities from oxygen atoms).

Hence, these electron density calculations further show that hydrogen does not diffuse into zirconia as considered in our oxygen potential model where it is presumed that the ZrO_2 acts as a physical barrier to hydrogen penetration.

6. CONCLUSIONS

1. A model based on a generalised Stefan-Maxwell treatment has been used to describe the multi-component transport of steam, hydrogen and stable fission-product gas in the fuel-to-clad gap of defective CANDU fuel rods during severe reactor accident conditions. The governing transport equations, which involve a system of coupled partial differential equations, have been solved using a finite-difference and control-volume methodology.

2. The model has been used to interpret the volatile (cesium) fission product release behavior, and the Zircaloy and fuel oxidation behavior, as observed in three high-temperature annealing experiments (from 1628 to 1915 K) in steam. For these experiments, mini-elements were fabricated from spent fuel samples and cladded in Zircaloy. The present analysis indicates that hydrogen produced from the Zircaloy oxidation reaction will significantly lower the oxygen potential so that significant fuel oxidation (and corresponding fission gas release) will not occur until after completion of the clad-oxidation process. When the oxidized cladding remains as a physical barrier, steam ingress is more difficult where it must diffuse against a counter-current flow of out-going fission gas and any hydrogen produced from urania oxidation. Local hydrogen production (from the internal fuel oxidation process) will also result in a reduced local oxygen potential in the fuel-to-clad gap compared to that which occurs in the bulk coolant.

3. During the initial Zircaloy oxidation phase in the CRL experiments, the model was able to predict the reduced fission product release kinetics as well as the timing for the completion of the clad-oxidation process. In this simulation, the model (with an effective gap size of 20 μm at temperature) was able to successfully predict whether single-sided or double-sided oxidation had occurred in accordance with the metallographic examination. However, in order to account for the observed release kinetics after the completion of clad oxidation, it was necessary to assume a greater atmospheric exchange due to possible cracking of the brittle oxide layer. With the assumption of cracking (by assuming a reduced path length for gas transport), the model was successfully able to reproduce the fission product release kinetics and the final fuel stoichiometry as determined from end-of-test weight gain measurements.

4. Semi-empirical atomistic simulations predict that the oxygen and hydrogen cannot diffuse effectively in a perfect bulk structure of ZrO_2. To account for the observed diffusivity of oxygen in zirconium dioxide, diffusion must be taking place through cracks or other planar defects. It was also found that while the oxygen can diffuse in ZrO_2, hydrogen will be trapped by oxygen atoms and thus prevented from diffusing into the bulk.

7. ACKNOWLEDGEMENTS

The present analysis was supported by the Natural Sciences and Engineering Research Council of Canada and the Department of National Defense (Director General of Nuclear Safety and Academic Research Program). The HCE2 experiment was sponsored by the CANDU Owners Group (Ontario Power Generation, Hydro Quebec, New Brunswick Power and Atomic Energy of Canada Limited). The authors would like to thank Dr. H.W. Bonin and C. Cole for assistance with the numerical solution, Drs. W.T. Thompson and F.C. Iglesias for many helpful discussions and Dr. O. Jepsen and MPI - Stuttgart for providing the TB-LMTO-ASA code.

REFERENCES

1. B.J. Lewis, C.R. Phillips and M.J. Notley, "A Model for the Release of Radioactive Krypton, Xenon, and Iodine from Defective UO_2 Fuel Elements," Nucl. Technol. 73 (1986) 72.
2. B.J. Lewis, F.C. Iglesias, D.S. Cox and E. Gheorghiu, "A Model for Fission Gas Release and Fuel Oxidation Behaviour for Defected UO_2 Fuel Elements," Nucl. Technol. 92 (1990) 353.
3. B.J. Lewis, "A Generalized Model for Fission-Product Transport in the Fuel-to-Sheath Gap of Defective Fuel Elements," J. Nucl. Mater. 175 (1990) 218.
4. B.J. Lewis, R.D. MacDonald, N.V. Ivanoff and F.C. Iglesias, "Fuel Performance and Fission Product Release Studies for Defected Fuel Elements," Nucl. Technol. 103 (1993) 220.
5. B.J. Lewis and H.W. Bonin, "Transport of Volatile Fission Products in the Fuel-to-Sheath Gap of Defective Fuel Elements During Normal and Reactor Accidents," J. Nucl. Mater. 218 (1994) 42.
6. P. Hofmann, "Current Knowledge on Core Degradation Phenomena, A Review," J. Nucl. Mater. 270 (1999) 194.
7. Z.W. Lian, L.N. Carlucci and V.I. Arimescu, "Convective-Diffusive Transport of Fission Products in the Gap of a Failed Fuel Element," Proceedings of the 15th Annual Conference of the Canadian Nuclear Society, Montreal, Quebec, June 5-8, 1994, Canadian Nuclear Society, 1994, Session 5C.
8. B.J. Lewis, "Prediction of the Oxygen Potential in the Fuel-to-Clad Gap of Defective Fuel Rods During Severe Reactor Accident Conditions," J. Nucl. Mater. 270 (1999) 221.
9. B.J. Lewis, B. André, B. Morel, P. Dehaudt, D. Maro, P.L. Purdy, D.S. Cox, F.C. Iglesias, M.F. Osborne and R.A. Lorenz, "Modelling the Release Behaviour of Cesium During Severe Fuel Degradation," J. Nucl. Mater. 227 (1995) 83.
10. B.J. Lewis, B.J. Corse, W.T. Thompson, M.H. Kaye, F.C. Iglesias, P. Elder, R. Dickson and Z. Liu, "Low Volatile Fission-Product Release and Fuel Volatilization During Severe Reactor Accident Conditions," J. Nucl. Mater. 252 (1998) 235.
11. B.J. Lewis, B. André, G. Ducros and D. Maro, "A Model for Non-Volatile Fission Product Release During Reactor Accident Conditions," Nucl. Technol. 116 (1996) 34.
12. D.R. Olander, "Thermodynamics of Urania Volatilization in Steam," J. Nucl. Mater. 270 (1999) 187.
13. F.C. Iglesias, B.J. Lewis, P.J. Reid and P. Elder, "Fission Product Release Mechanisms During Reactor Accident Conditions," J. Nucl. Mater. 270 (1999) 21.
14. D.R. Olander, "Materials Chemistry and Transport Modeling for Severe Accident Analyses in Light-Water Reactors, II: Gap Processes and Heat Release," Nucl. Eng. Des. 148 (1994) 273.
15. R.B. Bird, W.E. Stewart and E.N. Lightfoot, Transport Phenomena, John Wiley & Sons, New York (1960).
16. J. Rest and A.W. Cronenberg, J. Nucl. Mater. 150 (1987) 203.
17. J.R. Mathews and M.H. Wood, Nucl Eng. Des. 56 (1980) 439.
18. P.E. Blackburn, "Oxygen Pressures Over Fast Breeder Reactor Fuel (I) A Model for $UO_{2\pm x}$," J. Nucl. Mater. 46 (1973) 244.
19. B.J. Lewis, D.S. Cox and F.C. Iglesias, "A Kinetic Model for Fission Product Release and Fuel Oxidation Behavior for Zircaloy-Clad Fuel Elements Under Reactor Accident Conditions," J. Nucl. Mater. 207 (1993) 228.
20. L. Baker and L.C. Just, "Studies of Metal-Water Reaction at High Temperatures, Part III," ANL-6548 (1962).
21. V.F. Urbanic and T.R. Heidrick, "High-Temperature Oxidation of Zircaloy-2 and Zircaloy-4 in Steam," J.Nucl. Mater. 75 (1978) 251.
22. R.E. Pawal, J.V. Cathcart and R.A. McKee, "The Kinetics of Oxidation of Zircaloy-4 in Steam at High Temperature," J. Electrochem. Soc. 126 (1979) 1105.
23. J.T. Prater and E.L. Courtright, "Properties of Reactor Fuel Rod Materials at High Temperatures," Pacific Northwest Laboratory, NUREG/CR-4891, PNL-6164 (1987).
24. F.C. Iglesias, D.B. Duncan, S. Sagat and H.E. Sills, J. Nucl. Mater. 130 (1985) 36.
25. T. Yamashita, "Steam Oxidation of Zircaloy Cladding in the ORNL Fission Product Release Tests," NUREG/CR-4777 (ORNL/TM-10272), Oak Ridge National Laboratory (1988).
26. D.R. Olander, "Materials Chemistry and Transport Modelling for Severe Accident Analyses in Light-Water Reactors, I: External Cladding Oxidation," Nucl. Eng. Des. 148 (1994) 253.
27. D.R. Olander and V. Mubayi, "Review of the Materials-Chemistry Models in Victoria Code", J. Nucl. Mater. 270 (1999) 1.

28. T.J. Heames, D.A. Williams, N.E. Bixler, A.J. Grimley, C.J. Wheatley, N.A. Johns, P. Domagala, L.W. Dickson, C.A. Alexander, I. Osborn-Lee, S. Zawadzki, J. Rest, A. Mason and R.Y. Lee, "VICTORIA: A Mechanistic Model of Radionuclide Behaviour in the Reactor Coolant System Under Severe Accident Conditions," U.S. Nuclear Regulatory Commission, NUREG/CR-5545, SAND90-0756, Rev. 1, R3, R4, December 1992.
29. FTHEXP and CTHEXP sections from J.K. Hohorst (ed.), "SCDAP/RELAP5/MOD2 Code Manual, Volume 4: MATPRO - A Library of Materials Properties for Light-Water-Reactor Accident Analysis," USNRC report NUREG/CR-5273 (EGG-2555), 1990 February.
30. C. Callu, D. Baron and J.-M. Ruck, "EDF Fragment Relocation Model Based on the Displacement of Rigid Bodies," Fifth International Conference on CANDU Fuel, Toronto, Ontario, Canada, 1997 September 21-25, Volume 2, pp. 222-235.
31. M.G. Fontana, "Corrosion Engineering," Third Edition, McGraw-Hill Book Company, New York, 1986, p. 510-511.
32. M.I. Baskes, "Modified Embedded Atom Potentials for Cubic Materials and Impurities", Phys. Rev. B46 , 1992, 2727.
33. F.C. Iglesias, S. Sagat and H.E. Sills, "High Temperature Oxidation of Zircaloy", Res Mechanica 17, 1986, 125.
34. O.K. Andersen, O. Jepsen, and M. Sob, "Linearized Band Structure Methods" in "Electronic Band Structure and its Applications, edited by M. Yussouff, Springer Verlag, Berlin, 1986, 1-57.
35. J.K. Nørskov, "Chemisorption on Metal Surfaces", Rep. Prog. Phys. 53, 1990, 1253.

Table 1: Summary of Annealing Experiments for Mini-Element Test at CRL[9]

Conditions	HCE2-CM2	HCE2-CM6	HCE2-CM1
Pretest conditions:			
Element identity	AC-19	AC-19	AC-19
Discharge linear power (kW m^{-1})	32.1	32.1	32.1
Burnup (MWh/kgU)	457.2	457.2	457.2
Test description:			
Fuel specimen	UO_2/Zr-4	UO_2/Zr-4	UO_2/Zr-4
Initial enrichment (wt% ^{235}U in U)	1.38	1.38	1.38
Pellet diameter (mm)	12.15	12.15	12.15
UO_2 length (mm)	9	11	10
Specimen weight (g)	14.696[(b)]	16.890[(b)]	16.969[(b)]
Temperature (K)	1628	1768	1915
Environment[(a)]			
Temperature ramp (K/s)	0.9	0.9	0.9
Hold Steam (h)	2.5	2.5	2.5
Grain radius (μm)	3.5 to 21[(c)]	3.5 to 21[(c)]	3.5 to 21[(c)]

(a) Atmospheric conditions for temperature ramp: argon/2%H_2 at 400 mL min^{-1} argon at STP; temperature plateau: 60 g h^{-1} steam and 100 ml min^{-1} argon at STP.
(b) Includes the weight of the Zircaloy end caps (each cap weighed about 2.03 g and cladding 1.07 g).
(c) Based on grain size measurements of the as-received, irradiated fuel pellet (volumetrically averaged value is 6.5 μm). The grain size did not increase because of pinning by fission product bubbles.

Table 2: Model Parameters and Results for CRL Hot Cell Experiments

Test	Temperature (K)	Stoichiometry Deviation			Model Parameters		
		Calculated		Measured	S/V ratio (m^{-1})	Initial release fraction, g_o	Trapping fraction, ξ(%)
		End-of-test $x(t)$	Equilibrium, x_e	End-of-test			
CM2	1628	0.15	0.17	0.18	2.32	0.22	15
CM6	1768	0.16	0.16	0.16	2.08	0.25	15
CM1	1915	0.13	0.14	0.15	2.19	0.32	15

Table 3: Potential Parameters for the Zr-O-H system.[a]

	E_c (eV)	r_e (Å)	α	A	$\beta^{(0)}$	$\beta^{(1)}$	$\beta^{(2)}$	$\beta^{(3)}$	$t^{(0)}$	$t^{(1)}$	$t^{(2)}$	$t^{(3)}$
Zr	6.36	3.2	4.46	1.13	2.40	0.0	2.3	1.0	1.0	9.0	2.0	-4.0
O	2.558	1.21	6.49	1.5	6.49	6.49	6.49	6.49	1.0	0.09	0.1	0.0
H	2.235	0.74	2.96	2.5	2.96	3.0	3.0	3.0	1.0	0.20	-0.1	0.0

(a) Values listed are the cohesive energy E_c, the equilibrium nearest-neighbor distance r_e, the exponential decay factor α for the universal energy function, the scaling factor A for the embedding energy, the exponential decay factors $\beta^{(i)}$ for the atomic densities and the weighting factors $t^{(i)}$ for the atomic densities.

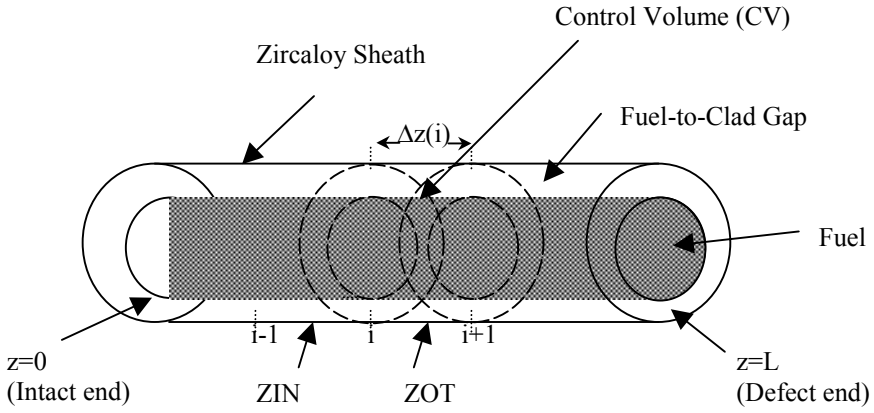

Figure 1. Schematic of a breached fuel rod with axial discretization (finite-difference mesh) and control volume grid used for the solution of the gap transport.

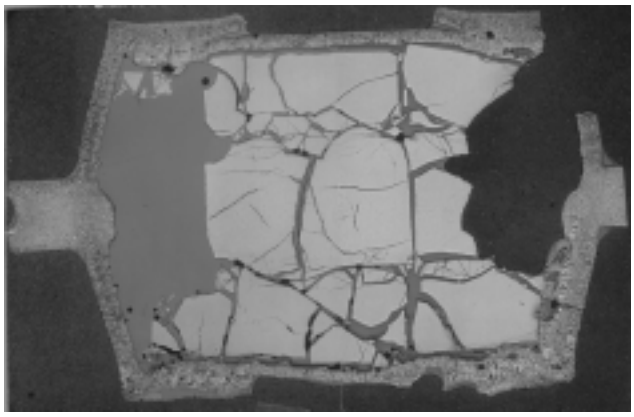

Figure 2. Post-test longitudinal ceramograph of the mini-element sample from the HCE2-CM1 test (HCE4 experiment; 42 kW m^{-1} peak linear power, 219 MWh/kgU burnup).

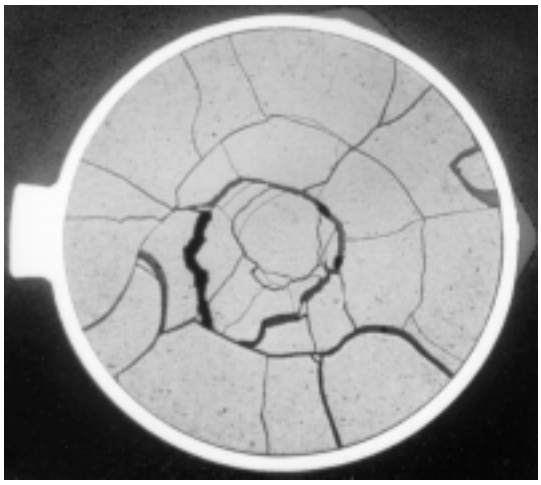

Figure 3. Transverse ceramograph of as-received Darlington fuel element Q53150C element #16 (HCE4 experiment; 42kWm^{-1} peak linear power, 219 MWh/kgU burnup).

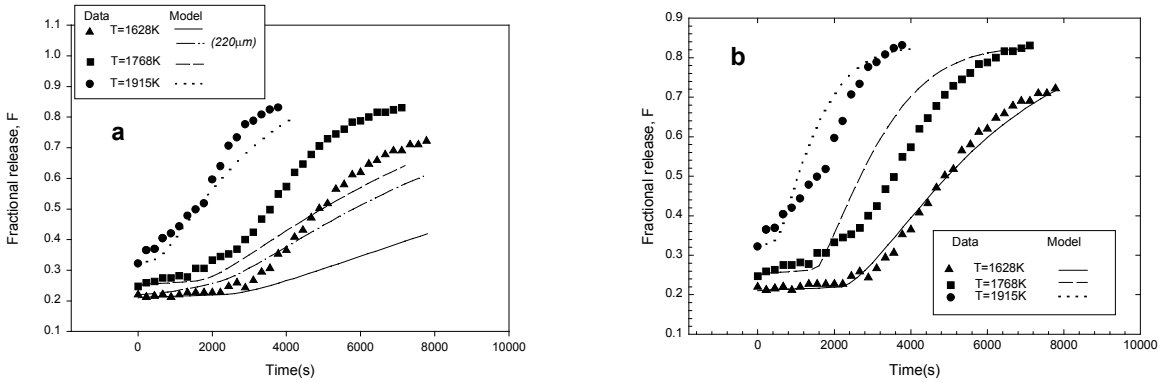

Figure 4. Fractional release as a function of time. The experimental points are for the CM2, CM6 and CM1 mini elements with corresponding temperatures: 1628K (triangles), 1768 K (squares and 1915 K (circles). The model simulations are shown assuming (a) an uncracked sheath and (b) a cracked sheath (see text).

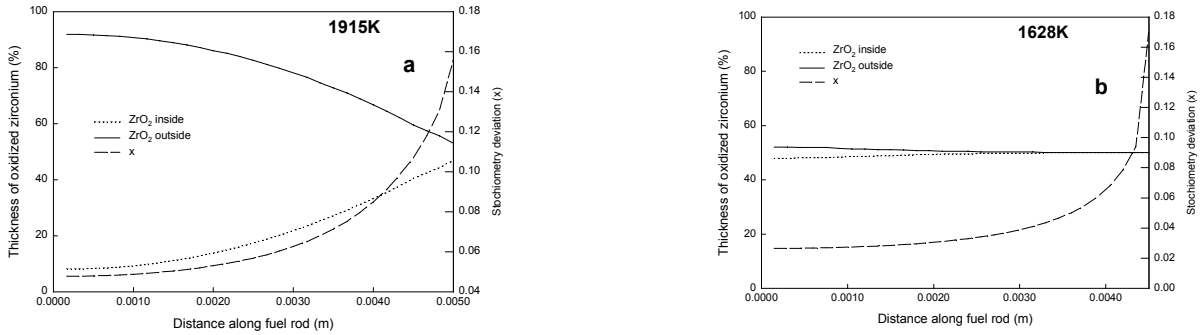

Figure 5. Internal and external oxidation profile for the cladding when clad oxidation is complete at (a) 1915 K (i.e., at 4200 s) and (b) 1628 K (i.e., at 7800 s). The stochiometry deviation at this time is also shown.

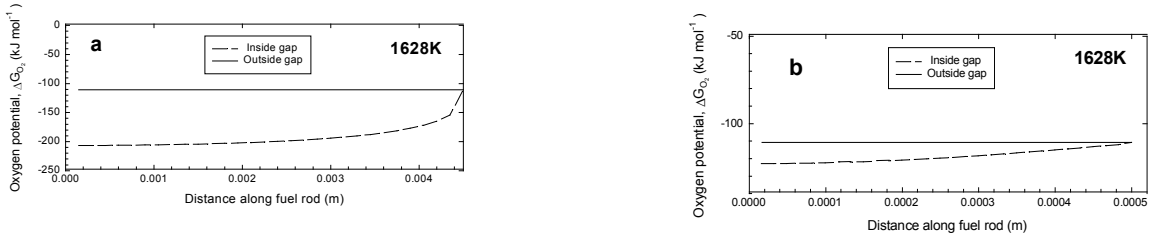

Figure 6. Calculated oxygen potential inside the gap and in the RCS outside the clad for the 1628 K simulation: (a) at the end of clad oxidation and (b) at the end of the experiment (i.e., at 7800 s) assuming a cracked sheath.

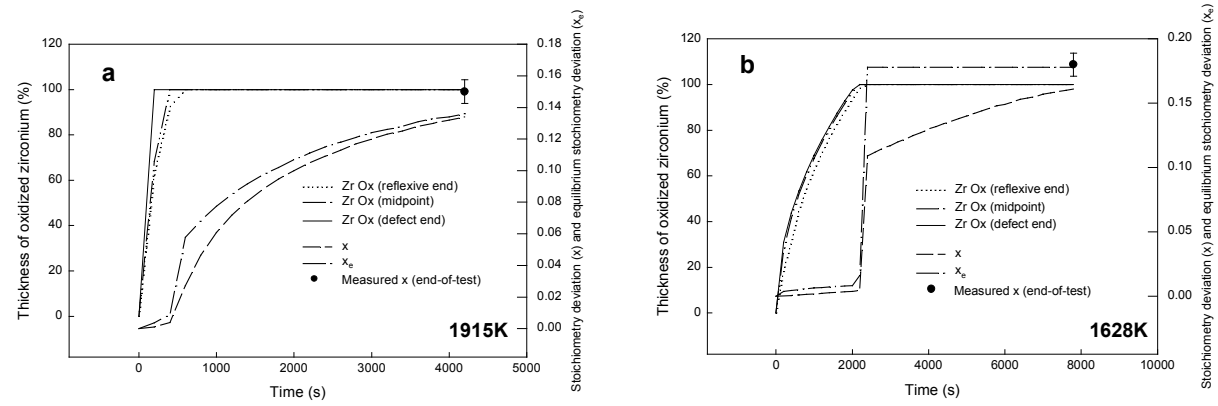

Figure 7. Calculated average stochiometry deviation (x), equilibrium stochiometry deviation (x_e) and thickness of oxidized zirconium at various places along the length of element as a function of time for the uncracked element (prior to complete zirconium oxidation) and a cracked element after clad oxidation for (a) CM1 (i.e., 2 cracks) and (b) CM2 (i.e., 8 cracks).

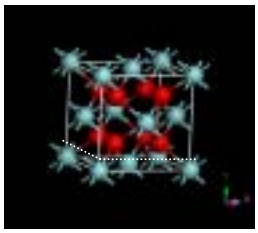

Figure 8. Unit cell of ZrO_2.

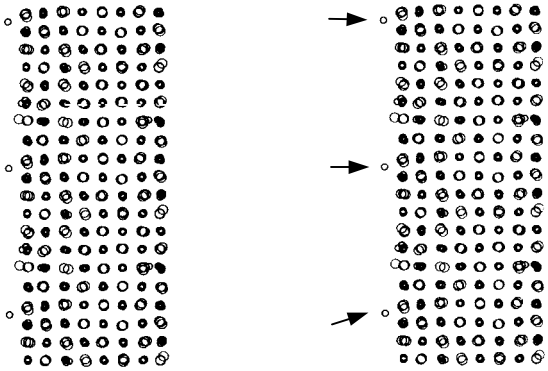

Figure 9. Slabs of ZrO_2 with 288 atoms and periodic boundary condition and 1700 K temperature. The atoms on the left (indicated by arrow) are oxygen atoms whose diffusion is studied. Bigger circles represent positions of zirconium atoms while the smaller ones are oxygen atoms.

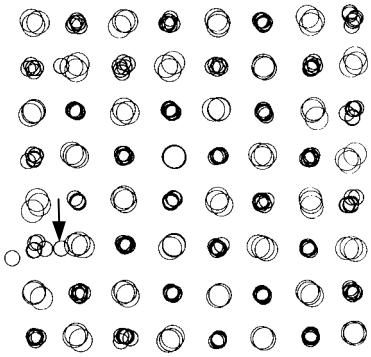

Figure 10. Slab of ZrO_2 as in Fig. 9 after 5000 psec.

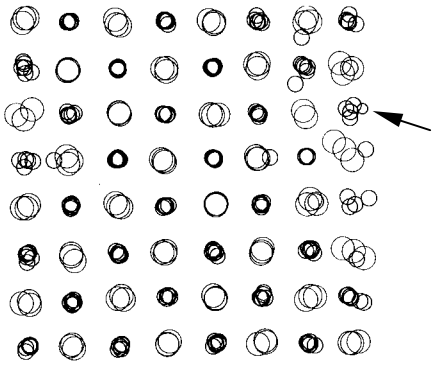

Figure 11. Slab of ZrO_2 with hydrogen atom bounded to oxygen atoms after 50 psec.

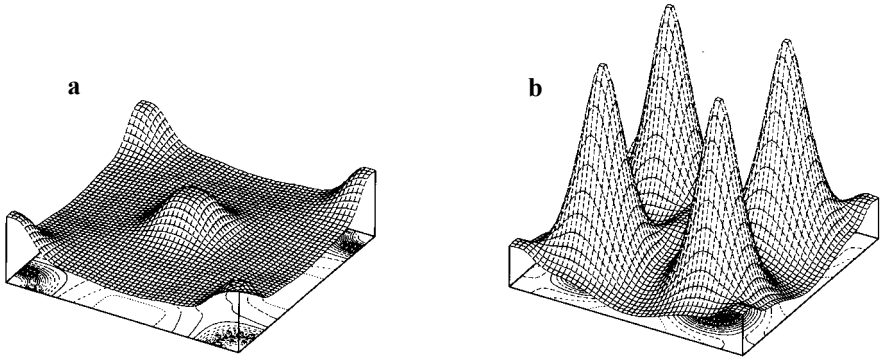

Figure 12. Electron charge density for zirconium (a) and zirconia (b) calculated using the LMTO-ASA method[34].